K-shell ionization of intermediate-Z elements by 30-MeV/amu H, N, Ne, and Ar ions

V. Horvat,* G. Sampoll, K. Wohrer,† M. Chabot,† and R. L. Watson
Cyclotron Institute, Texas A&M University, College Station, Texas 77843-3366
and Department of Chemistry, Texas A&M University, College Station, Texas 77843-3366
(Received 31 January 1992)

Cross sections for K x-ray production in solid targets ($Z=13$, 22, 26, 29, 32, 40, 42, 46, and 50) by 30-MeV/amu beams of H, N, Ne, and Ar were measured. The cross sections were determined by recording the spectra of K x rays with a Si(Li) detector in coincidence with beam particles detected in a microchannel plate assembly. The K-shell-ionization cross sections deduced from these data agree quite well with the predictions of the perturbed-stationary-state theory with energy loss, Coulomb deflection, and relativistic corrections. Detailed analyses of the projectile and target Z dependences of the cross sections were performed. Also, the relative intensities of K x rays from double K-shell ionization of the higher-Z targets are presented for N, Ne, and Ar projectiles.

PACS number(s): 34.50.Fa, 32.30.Rj

I. INTRODUCTION

Although the first investigations of K-shell ionization by heavy charged particles were conducted over 50 years ago, many of the details of the ionization process are not yet fully understood. Interest in this subject continues to inspire developments in the theoretical description of ionization mechanisms, as well as applications that require accurate databases of ionization cross sections. Most of the experimental data on K-shell ionization collected so far were obtained using protons and α particles in the energy region below 10 MeV/amu. A comprehensive list of pertinent reviews and references is given in the cross-section compilation of Lapicki [1]. Very few investigations of K-shell ionization induced by heavy ions in the intermediate- and high-energy region have been carried out because there are not many particle accelerators available that can provide the necessary beams.

The mechanisms that contribute to the production of K-shell vacancies in heavy-ion–atom collisions are numerous, and their relative importance depends on the values of the many parameters that characterize the process. A universal theory covering all the possible parameter regimes still does not exist, but most of the available experimental data for low-Z projectiles, spanning a large range of relative velocities and target atomic numbers, are successfully described in a consistent way by a perturbed stationary-state theory with energy loss, Coulomb deflection, and relativistic corrections (ECPSSR). This formulation utilizes the plane-wave Born approximation in treating direct K-shell ionization [2] and the Oppenheimer-Brinkman-Kramers (OBK) approach in calculating the contribution of K vacancies produced by nonradiative K-electron capture to the projectile [3]. In addition, it takes into account the Coulomb deflection of the projectile, the recoil of the target atom, the increased binding of the target K-shell electrons due to the projectile nuclear charge, and the polarization of the electrons in the target atoms. The ECPSSR formulation is nonrelativistic, but it incorporates corrections for relativistic effects.

While the ECPSSR theory has been rather thoroughly tested with low-Z projectiles below 10 MeV/amu, it is not known how well it works for intermediate- and high-energy heavy ions. One important benchmark has been established by Liatard *et al.* [4], who recently performed measurements on solid targets ranging in Z from 27 to 90 using 30-MeV/amu Ne and Ar projectiles. Their results, while yielding good overall agreement with the predictions of the CPSSR theory (an earlier version of the ECPSSR theory, which did not take into account the recoil of the target atom), displayed small but systematic deviations from the theoretical projectile and target-Z dependences. They also revealed that K-electron capture to the projectile contributed significantly to the total K-shell-ionization cross sections for Ar.

The measurements described in this paper were undertaken to further examine the projectile and target-Z dependences of K-shell ionization at 30 MeV/amu. Ionization cross sections have been determined from the yields of K x rays produced in solid targets ranging from $Z=13$ to 50 by beams of H, N, Ne, and Ar ions. The regions spanned by the present data and those of Liatard *et al.* are shown in Fig. 1, where the charge asymmetry parameter $\alpha=Z_1/Z_2$ is plotted versus the adiabaticity parameter $\eta=(v_1/v_K)^2$. (The quantities Z_1, Z_2, v_1, and v_K are, respectively, the atomic numbers of the projectile and target, and the velocities of the projectile and the K electron of the target.) The region of proven validity of the ECPSSR formulation is indicated by the diagonal lines. It is evident from Fig. 1 that the data obtained in this study partially overlap with those of Liatard *et al.*, thereby providing a check of the consistency of the two data sets.

II. EXPERIMENTAL METHODS

Beams of 30-MeV/amu HD^+, N^{5+}, Ne^{7+}, and Ar^{14+} were extracted from the Texas A&M K500 superconducting cyclotron, directed through an analyzing magnet, and focused to a spot size less than 1 mm diameter by viewing a ZnS phosphor mounted in the target holder

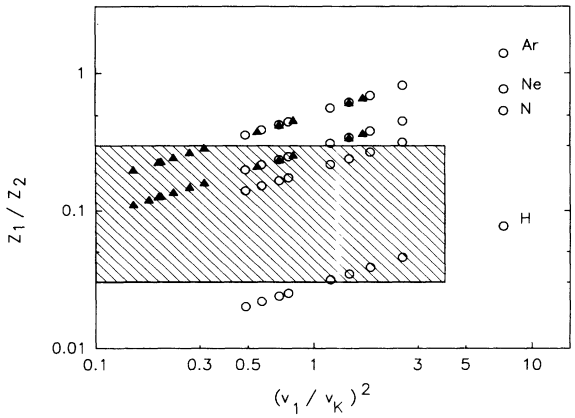

FIG. 1. Region covered by the present work (open circles) and that of Liatard *et al.* [4] (solid triangles) in terms of the asymmetry parameter ($\alpha = Z_1/Z_2$) and the adiabaticity parameter ($\eta = [v_1/v_K]^2$) for the various projectiles specified. The area containing the diagonal lines is the region of proven validity of the ECPSSR formulation.

with a television camera. The HD^+ beam was converted to an H^+ beam by means of a stripper foil placed upstream from the analyzing magnet. A 2.5-cm-long carbon collimator with a 3-mm-diam opening was positioned 4.5 cm in front of the target to prevent scattered beam particles from hitting the target and to limit changes in the detection solid angle due to movement of the beam. The beam intensity was regulated using three pairs of remotely adjustable slits, all located upstream from the analyzing magnet. The vacuum in the target chamber was maintained below 5×10^{-5} Torr.

The targets were mounted on a target wheel that was coupled to a remotely controlled stepping motor. A list of the targets used in the experiments is given in Table I. All of the targets were self-supporting, commercially available, 25-μm-thick metal foils except the Ge target, which was prepared by vacuum evaporation onto a 6-μm (1.62-mg/cm^2)-thick Al foil. The nominal error in target thickness was 10% for the metal targets and 20% for the germanium target. No impurities were detected in the targets, but a small amount of iron was found in the aluminum backing of the germanium target. However, this did not interfere with the measurements. The angle between the beam axis and the target plane was 45°.

A Si (Li) detector was positioned at 90° with respect to the beam axis and viewed the front surface of the target

TABLE I. Targets used in the experiments.

Target element	Effective thickness (mg/cm^2)
Al	9.542
Ti	15.98
Fe	27.85
Cu	31.65
Ge	0.1882
Zr	23.01
Mo	36.13
Pd	42.50
Sn	25.50

at an angle of 45° relative to the surface normal through a 1.3×10^{-3}-cm-thick beryllium window. The detector cryostat was coupled directly to the target vacuum chamber with a distance of 2.5 cm between the detector (Si) crystal and the target. The Si crystal was cylindrical and had an active area of 30 mm^2 and an active thickness of 3 mm. It gave an energy resolution of 260-eV full width at half maximum (FWHM) at 6.4 keV.

The efficiency of the Si (Li) detector was determined using an ^{241}Am calibration source mounted on the target wheel in the target position. The measured intensities of the x rays were corrected for absorption in the polyethylene foil that covered the source. The thickness of the cover foil was determined directly with a micrometer as well as by measuring the transmission of low-energy x rays from other sources. The x rays from the calibration source also were measured through the back surface to check that the thickness of the front and back cover foils were the same. Self-absorption in the calibration source was calculated from the measured relative intensities of the x rays from the calibration source and from another ^{241}Am (alpha) source in which the self-absorption was negligible. In order to extend the efficiency curve below 3.3 keV, it was necessary to determine the thicknesses of other absorption layers between the detector's active area and the source. The thicknesses of the beryllium window and the gold surface layer on the Si crystal (approximately 4×10^{-5} g/cm^2) were used to calculate the absorption corrections. The thickness of the silicon dead layer and the solid angle of detection were determined from the absolute intensities of the x rays from the source. Since no discontinuities were found in the absorption curve near the points of interest, the absorption corrections were applied to the integrated photopeak areas in the usual manner. The escape of Si K x rays through the front surface of the detector crystal was taken into account using the expression derived by Fioratti and Piermattei [5] (including the factor of 0.5 that was omitted in the original publication). The absorption coefficients, densities, and atomic weights used to calculate the various corrections were taken from McMaster *et al.* [6]. The energies and relative intensities used for the x rays and γ rays from ^{241}Am, and the K-shell fluorescence yields used for the targets, were those given in the tables of Lederer and Shirley [7] except for the energy and relative intensity of the Np M x ray, which was taken from the work of Hansen *et al.* [8].

A microchannel plate detector (MCPD) in Chevron configuration was placed 5 cm behind the target directly in the beam path to count the beam particles in coincidence with the K x rays. The MCPD signals were fed directly into a fast amplifier, without going through a preamplifier. Radiation damage to the MCPD was not a problem during the measurements since the beam intensity was kept below the level at which significant damage occurs. The main limitation on the beam intensity was imposed by the desire to maintain the counting rate in the x-ray spectrometer at or less than 1000 counts/s. The x-ray counting rate was monitored continuously by means of a rate meter and it could be adjusted by changing the slit openings. The corresponding beam intensity

(which was dictated by x-ray detector solid angle, the target thickness, and the K-shell x-ray production cross section) was in most cases well below 10^5 particles/s. The counting rate of the MCPD was the limiting factor only in the measurements with the thin Ge target and with H projectiles.

As a consequence of the coincidence requirement, the background was reduced and the need to measure the efficiency of the MCPD was eliminated. However, in two of the runs, duplicate measurements were performed; one with the MCPD, and the other with a silicon surface barrier detector in its place. From a comparison of the data from these two runs, it was concluded that the efficiency of the MCPD was essentially 100% for 30-MeV/amu Ar and N projectiles. This conclusion was confirmed in the analysis of the data taken in all the other measurements by comparing the (simultaneously accumulated) x-ray coincidence and singles spectra.

A schematic diagram of the electronic system used in the present experiment is shown in Fig. 2. Singles spectra were accumulated using an IBM XT computer with a Nucleus PC analyzer card and the accompanying software. The coincidence requirement was imposed by means of a time-to-amplitude-converter–single-channel-analyzer (TAC-SCA) unit and the coincidence spectra were recorded via a PC(386)-based CAMAC multiparameter data acquisition system (MPDAS) that utilized Kinetic Systems hardware (PC card, CAMAC crate and controller) and various CAMAC modules [an eight-unit analog-to-digital converter (ADC) module, a digital-to-analog converter (DAC), and a multichannel scaler]. The x-ray detector provided the start signals for the TAC-SCA and the MCPD provided the stop signals. The x-ray energy signals were sent to one of the ADC's and the TAC analog signals were sent to another. After each run, the data were stored on a hard disk drive containing removable disk packs. Accumulation of the singles spectra was controlled using a gate-busy signal from the MPDAS DAC, thereby insuring that the counting period was synchronized with that of the MPDAS. With the multichannel scaler of the MPDAS, it was possible to measure (and monitor) the live time of the system, the

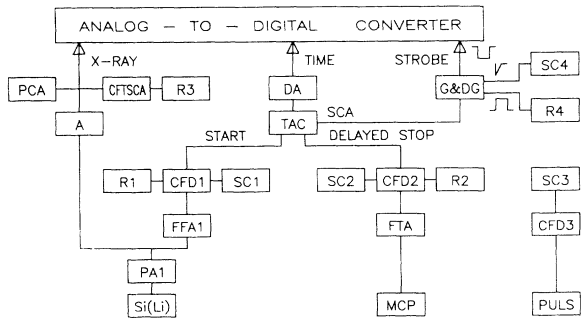

FIG. 2. Schematic diagram of the electronic system. (PCA, personal computer pulse-height analyzer; CFTSCA, constant fraction timing single-channel analyzer; A, linear amplifier; DA, delay amplifier; TAC, time-to-amplitude converter; G&DG, gate and delay generator; CFD, constant fraction discriminator; SC, scaler; FFA, fast filter amplifier; FTA, fast timing amplifier; PULS, pulser; PA, preamplifier; R, rate meter.)

fraction of nonaccepted events, and the particle, x-ray, and coincidence counting rates.

The time resolution of the system was 15-ns FWHM and the number of random coincidences was very small compared to the number of true coincidences. The background in the TAC spectrum displayed a periodic pattern of peaks, each of which was separated by 57 ns, caused by accidental coincidences with beam pulses other than the ones that produced the detected x rays. These peaks were very small, since the beam intensity was low enough that, on average, only one particle passed through the target per 2000 beam pulses (i.e., per 100 μs).

The time resolution and true-to-random coincidence ratio became worse as the target atomic number decreased because of the relatively larger time jitter associated with the lower voltage signals. However, this did not significantly affect the measurements. The timing signals for Al targets (K x-ray energy = 1.5 keV) could not be separated from the noise, and hence it was not possible to perform coincidence measurements for this target. Therefore, the K-shell-ionization cross sections for Al were measured relative to those for Cu by placing an Al target in front of a Cu target and recording the combined singles spectra. In the analysis of the data, the absorption of Cu K x rays in the Al target and the fluorescence of Al x rays were taken into account.

III. CALCULATIONS

A FORTRAN program was written to calculate K-shell-ionization cross sections using the ECPSSR theoretical formulation. Two data files were constructed; one with the target atomic weights, K-shell binding energies [9], and K-shell fluorescence yields [10] for all Z from 1 to 103, and the other one with the plane-wave-Born-approximation universal excitation function values as given by Rice, Basbas, and McDaniel [11].

The program gives the values of all the defined variables and allows for the exclusion of any number of effects from the calculations, so that it is possible to compare the results with all previously published calculations, including those based on the predecessors of the ECPSSR formulation, which took into account some, but not all, of the effects included in the ECPSSR theory. The results of the program were also checked by comparing them with the ECPSSR calculations of Lapicki [1] in his compilation of measured and calculated values of the K-shell ionization cross sections for the systems involving hydrogen- and helium-ion projectiles. The current program results satisfactorily reproduced the Lapicki results for all the cases that were checked.

The program was written for a PC(386), but it can be run on any machine (after compiling and linking). It is available from the authors upon request.

IV. DATA ANALYSIS

The data, which during the measurements had been stored on disk event by event, were analyzed off line using customized software for selecting and fitting the data. For each run, the total number of particles and the live-time fraction were determined from the scaler readings.

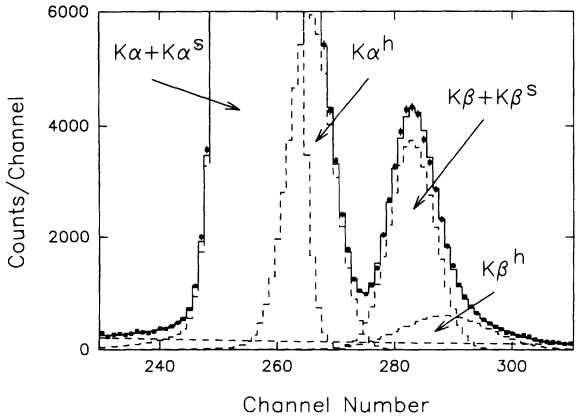

FIG. 3. A portion of a spectrum of Cu K x rays emitted during bombardment by 30-MeV/amu Ar ions. The results of a peak fitting analysis are shown by the dashed lines.

This latter quantity was obtained by taking the ratio of the number of accepted events to the number of coincidences. The true coincidence fraction was determined from the data recorded by the TAC ADC in coincidence with x-ray events falling within the $K\alpha$ and $K\beta$ peaks. The number of true coincidence $K\alpha$ x rays was determined by fitting the x-ray spectrum.

Part of the spectrum of K x rays emitted from a Cu target under bombardment by 30-MeV/amu Ar ions is shown in Fig. 3. This spectrum shows the principal $K\alpha$ and $K\beta$ peaks, which are shifted to higher energies than the normal (single-vacancy) diagram lines due to the presence of additional vacancies in the L and M shells, and two smaller peaks that arise from $K\alpha$ and $K\beta$ emission from atoms having double-K-shell vacancies. The former are generally referred to as $K\alpha$ and $K\beta$ satellites and the latter as $K\alpha$ and $K\beta$ hypersatellites. By comparing the measured energy shifts of these peaks with the results of Dirac-Fock calculations, the number of L vacancies present at the time of K x-ray emission may be estimated [12]. In applying fitting procedures to analyze the structure of the x-ray peaks, the hypersatellite peaks were assumed to be present in all the spectra except those taken with H projectiles. The fitting functions employed Gaussians with exponential tails on their low-energy sides to represent the x-ray peaks and the background was usually approximated by a second-order polynomial.

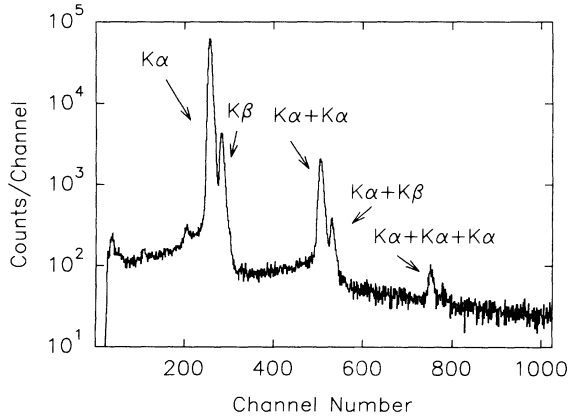

FIG. 4. The full x-ray spectrum from which Fig. 3 was taken. In addition to the Cu $K\alpha$ and $K\beta$ x-ray peaks, two sets of pileup peaks are present.

The full Cu spectrum, from which Fig. 3 was constructed, is shown in Fig. 4. Even though the counting rate in the x-ray detector was kept below 1000 counts/s, the spectrum displays two very pronounced groups of pileup peaks. These peaks are present because the K x-ray production cross section for this system was relatively large and the target was fairly thick, causing a large number of K x rays to be produced during the passage of a single projectile. Under these circumstances, the probability that two or even three x rays were detected simultaneously was quite large. Since the intensities of the pileup peaks was significant in most of the cases studied, their contributions had to be taken into account in the analysis of the peak intensities and their conversion to cross sections. The largest pileup correction (which was for the spectrum shown in Fig. 4) was 9%.

Another effect that had to be considered was the strong absorption of the $K\beta$ hypersatellite peak and some components of the $K\beta$ satellite peak in cases where their energies exceeded the K-binding energy [13]. This effect was especially pronounced in the thicker targets, as is demonstrated in Fig. 5. Here, the Cu K x-ray spectrum from Fig. 3 is compared with a spectrum obtained under the same conditions using a target that was thinner by a factor of 10. This effect introduced large uncertainties in the determination of the intensities of the $K\beta$ peaks. Therefore, only the $K\alpha$ peaks were used in the determination of the K-shell-ionization cross sections. The error introduced by this procedure is small because the $K\beta$-to-$K\alpha$ intensity ratio is of the order of 20% or less, so that even a 30% error in the value of the $K\beta$-to-$K\alpha$ intensity ratio employed in the analysis yields only a 5% relative error in the extracted total K x-ray intensity. The magnitude of this error decreases with the target and projectile atomic numbers.

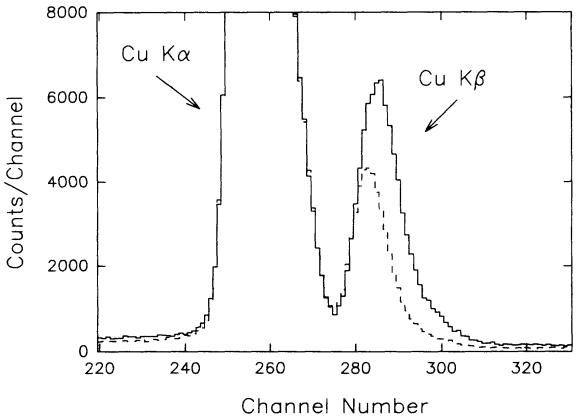

FIG. 5. Effect of increased absorption of the Cu $K\beta$ x rays caused by L-shell ionization. The solid line shows the x-ray spectrum obtained with a 3.22-μg/cm^2 target, while the dashed curve shows the x-ray spectrum obtained with 31.7-mg/cm^2 target. The two spectra have been normalized to equal $K\alpha$ peak intensities.

The fluorescence yields were assumed to be the same as those for single-vacancy atoms, since it was found that even elaborate calculations of this parameter involve a number of questionable approximations for multiply ionized atoms in a solid [4]. However, it should be noted that $\langle n_L \rangle$, the average number of L vacancies produced in K-shell-ionizing collisions, increases with projectile atomic number, approaching the value of 1 for $Z_1=10$ and the value of 2 for $Z_1=18$ at 30 MeV/amu [4]. The corresponding increase in the fluorescence yield, as estimated using the scaling procedure of Larkins [14], ranges from 3% for fifth-row elements up to 20% for Al when $\langle n_L \rangle=2$. The fluorescence yield increases are about a factor of 2 less than this when $\langle n_L \rangle=1$. In the case of Al, the error associated with the single-vacancy fluorescence yield is estimated to be $\approx 10\%$ [10].

The average projectile energies in the targets were calculated using the stopping-power tables of Hubert, Bimbot, and Gauvin [15]. Each experimentally determined K-shell-ionization cross section was multiplied by the theoretical (ECPSSR) cross sections for 30-MeV/amu projectiles and divided by the theoretical cross section for the actual average projectile energy to correct it for projectile energy loss. The maximum correction (30-MeV/amu Ar projectiles on Cu) was 5%, and it was opposite in sign to the correction for pileup.

Self-absorption was significant for all of the targets. Corrections for this effect ranged from 13% in Sn to 75% in Al. Other sources of attenuation played a role in only two cases: all measurements with the Al target, which had a copper target mounted behind it, and the measurements for Ge with the H beam. In the first case, the transmission of Cu x rays (used to normalize the Al x-ray yield) through the Al target was 62%, and in the second case, in which Al x rays from the Ge target backing were used to normalize the Ge x rays, the transmission of Al x rays was 28%. The Al x-ray normalization was employed in the latter case because the Ge target was too thin to give a measurable coincidence rate with H projectiles.

The K-shell-ionization cross sections were calculated using the following expression:

$$\sigma_K = \left[\frac{A}{N_A \rho d \omega_K f_\alpha}\right]\left[\frac{N_\alpha(\text{coinc})}{N_p R_L}\right]\left[\frac{R(\text{coinc})}{(\Omega\epsilon)_\alpha T_s T_a}\right], \quad (1)$$

where A is the atomic weight of the target, N_A is Avogadro's number, ρ is the target density, d is the target thickness corrected for the angle of inclination, ω_K is the target K-shell fluorescence yield, f_α is the $K\alpha$ intensity fraction, N_α(coinc) is the number of counts in the peaks containing the $K\alpha$ diagram plus satellite lines and the $K\alpha$ hypersatellite lines (corrected for pileup) in the coincidence spectrum, N_p is the number of projectiles, R_L is the live-time fraction, R(coinc) is the coincidence fraction, Ω is the x-ray detector solid angle, ϵ is the x-ray detector efficiency, T_s is the x-ray transmission factor within the target, and T_a is the x-ray transmission factor for any absorbers between the target and the detector. Taking into account all of the sources of error discussed above, it was concluded that the average error associated with the K-shell ionization cross sections deduced from the present measurements was $\pm 17\%$.

V. RESULTS AND DISCUSSION

A comparison between the experimental and the calculated (ECPSSR) K-shell-ionization cross sections is given in Fig. 6 and in Table II. The cross section ratio $\sigma_K(\text{expt})/\sigma_K(\text{ECPSSR})$ is shown in Fig. 7. In general, the agreement between the present results and the ECPSSR predictions is quite good, except in the region around $Z_2=30$ for Ar projectiles.

In order to examine the target and projectile Z dependences of the measured ionization cross sections in more detail, the scaled cross sections σ_K/Z_1^2 for N, Ne, and Ar projectiles divided by the cross sections for H projectiles are shown in Fig. 8. It is evident that the data display significant deviations from the simple Born-approximation Z_1^2 scaling law for all the projectiles. The experimental data obtained in the present work are all larger than unity except those for Al, which indicate that a crossover to values less than unity occurs in the vicinity of $Z_2=13$. The cross sections of Liatard *et al.* [4] for Ar and Ne projectiles have been divided by the ECPSSR cross sections for protons and these ratios (included in Fig. 8) indicate that another crossover occurs in the vicinity of $Z_2=60$. The cross-section ratios predicted by the ECPSSR calculations are shown by the dashed curves in Fig. 8. The agreement with the experimental ratios is within experimental error for all projectile-target combinations except Ar on Al and Ar on Z_2 from 26 to 40.

The reason for the Al deviation is not known at this time. It should be noted that increasing the fluorescence yield to correct for multiple-L-shell ionization causes the deduced cross section to drop even further below the ECPSSR curve. The deviations around $Z_2=30$, however, can be explained by considering the relative contribution to the total target K-shell-ionization cross section of electron transfer from the target K shell to the projectile K shell [EC(K)]. As shown in Fig. 9, the (theoretical) rel-

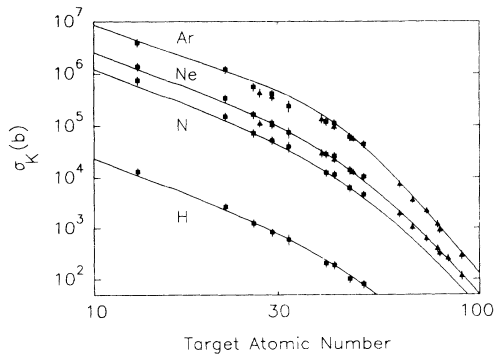

FIG. 6. K-shell-ionization cross sections as functions of the target atomic number for Ar, Ne, N, and H projectiles. The present data are shown by squares, the data of Liatard *et al.* [4] by triangles, and the results of the ECPSSR calculations by solid curves.

TABLE II. K-shell-ionization cross sections in units of 10^{-24} cm^2. (The average error in the cross sections determined in the present work is ±17%.)

Projectile	Target	Present	Ref. [4]	ECPSSR
H	Al	1.3×10^{4}		1.10×10^{4}
	Ti	2.7×10^{3}		2.27×10^{3}
	Fe	1.3×10^{3}		1.29×10^{3}
	Cu	8.3×10^{2}		8.74×10^{2}
	Ge	5.9×10^{2}		6.01×10^{2}
	Zr	2.0×10^{2}		2.31×10^{2}
	Mo	1.9×10^{2}		1.85×10^{2}
	Pd	1.0×10^{2}		1.18×10^{2}
	Sn	8.0×10^{1}		7.60×10^{1}
N	Al	7.5×10^{5}		5.71×10^{5}
	Ti	1.5×10^{5}		1.24×10^{5}
	Fe	7.2×10^{4}		7.15×10^{4}
	Cu	5.2×10^{4}		4.85×10^{4}
	Ge	4.0×10^{4}		3.32×10^{4}
	Zr	1.3×10^{4}		1.26×10^{4}
	Mo	1.1×10^{4}		9.92×10^{3}
	Pd	6.2×10^{3}		6.22×10^{3}
	Sn	4.6×10^{3}		3.91×10^{3}
Ne	Al	1.4×10^{6}		1.21×10^{6}
	Ti	3.4×10^{5}		2.74×10^{5}
	Fe	1.6×10^{5}		1.61×10^{5}
	Co		1.1×10^{5}	1.42×10^{5}
	Cu	1.1×10^{5}	1.0×10^{5}	1.10×10^{5}
	Ge	7.4×10^{4}		7.60×10^{4}
	Y		2.9×10^{4}	3.23×10^{4}
	Zr	2.8×10^{4}		2.86×10^{4}
	Mo	2.6×10^{4}	2.2×10^{4}	2.24×10^{4}
	Pd	1.4×10^{4}		1.38×10^{4}
	Ag		1.3×10^{4}	1.22×10^{4}
	Sn	1.0×10^{4}		8.53×10^{3}
	Sm		1.9×10^{3}	2.12×10^{3}
	Ho		1.0×10^{3}	1.23×10^{3}
	Ta		6.2×10^{2}	6.46×10^{2}
	Pt		4.0×10^{2}	3.86×10^{2}
	Au		3.2×10^{2}	3.49×10^{2}
	Bi		2.5×10^{2}	2.35×10^{2}
	Th		1.2×10^{2}	1.21×10^{2}
Ar	Al	3.9×10^{6}		4.27×10^{6}
	Ti	1.2×10^{6}		1.11×10^{6}
	Fe	5.6×10^{5}		7.12×10^{5}
	Co		4.3×10^{5}	6.41×10^{5}
	Cu	4.1×10^{5}	3.6×10^{5}	5.19×10^{5}
	Ge	2.4×10^{5}		3.75×10^{5}
	Y		1.3×10^{5}	1.65×10^{5}
	Zr	1.2×10^{5}		1.46×10^{5}
	Mo	1.1×10^{5}	9.6×10^{5}	1.13×10^{5}
	Pd	6.1×10^{4}		6.74×10^{4}
	Ag		5.6×10^{4}	5.90×10^{4}
	Sn	4.4×10^{4}		3.94×10^{4}
	Sm		7.4×10^{3}	8.02×10^{3}
	Ho		3.6×10^{3}	4.27×10^{3}
	Ta		2.2×10^{3}	2.07×10^{3}
	Pt		1.2×10^{3}	1.16×10^{3}
	Au		9.2×10^{2}	1.04×10^{3}
	Th		2.9×10^{2}	3.28×10^{2}

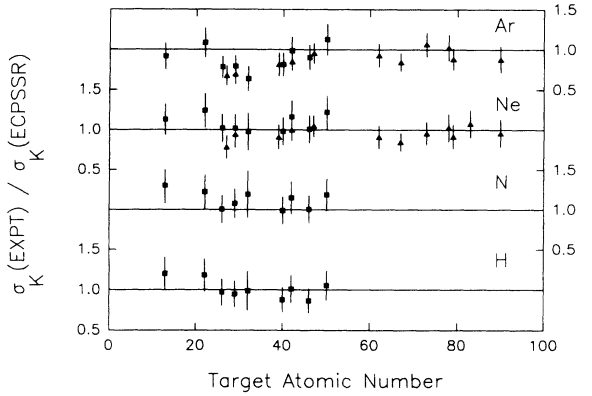

FIG. 7. Experimental K-shell-ionization cross section divided by the calculated (ECPSSR) cross section as a function of target atomic number for each of the projectiles used in this study. The present results are shown by squares and the results of Liatard *et al.* [4] by triangles.

ative EC(K) contribution is quite large in the vicinity of $Z=30$ and reaches its maximum value around $Z=40$. In the ECPSSR calculations, it was assumed that the projectile was fully stripped and, therefore, that all of the projectile K-shell states were available to capture K electrons from the target. In reality, the average projectile charge changes from its initial value (e.g., 14+ in the case of Ar) to its equilibrium value at some depth within the target. The charge distributions for 26-MeV/amu Ar^{13+} and

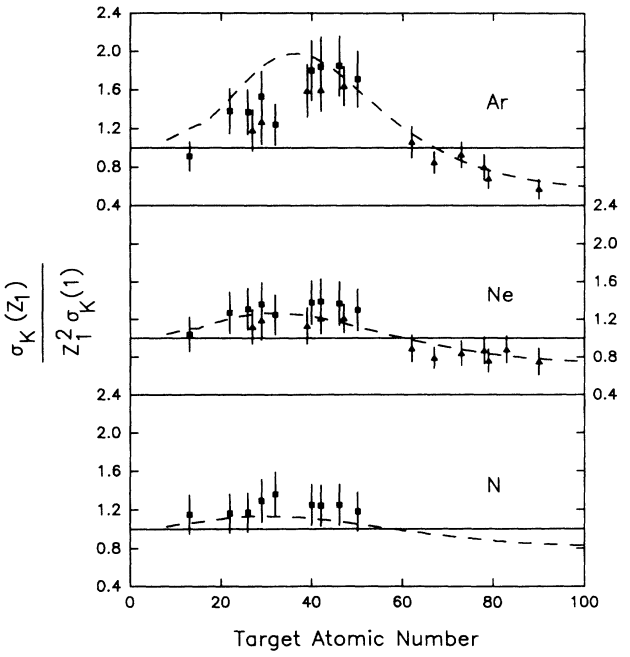

FIG. 8. Scaled experimental K-shell-ionization cross section σ_K/Z_1^2 divided by the cross section for protons as a function of the target atomic number for Ar, Ne, and N projectiles. The present results are shown by squares. The cross sections of Liatard *et al.* [4] have been divided by proton cross sections calculated using the ECPSSR formulation and are shown by triangles. The calculated (ECPSSR) ratios are shown by dashed curves.

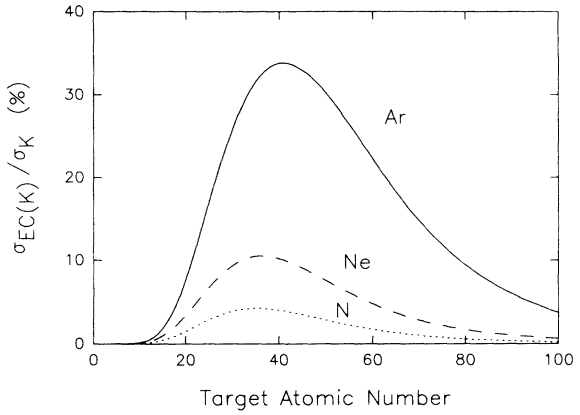

FIG. 9. Calculated relative contribution to the total K-shell-ionization cross section of electron transfer from the target K shell to the projectile K shell.

Ar^{18+} have recently been measured as a function of carbon target thickness by Awaya *et al.* [16]. These measurements show that although the average charge of the equilibrated beam is very close to 18+, the carbon thickness required to reach equilibrium is $\approx 1-5$ mg/cm^2. Moreover, in the case of Ar^{13+}, the average charge changes from approximately 16.9 at 0.1 mg/cm^2 to 17.9 at 0.5 mg/cm^2. Therefore, unless the charge distributions are quite different for targets with $Z>6$, it must be concluded that the average charge of the Ar beam used in the present measurements was less than 18 over a significant fraction of the x-ray production path length. Under these conditions, the resulting K-shell-ionization cross sections would reflect the reduced contribution from EC(K) due to the partial occupancy of the projectile K levels, and hence the cross sections deduced from these measurements would be lower than those predicted by the ECPSSR calculations. The effect should be especially prominent for the Ge target, which was much thinner

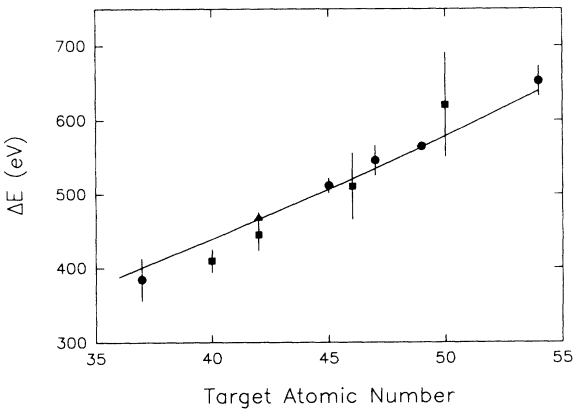

FIG. 10. Measured energy differences ΔE between the peaks containing the $K\alpha$ hypersatellite lines and the peaks containing the $K\alpha$ diagram plus satellite lines for the four highest-Z targets examined in the present work (squares). $K\alpha$ hypersatellite energy shifts determined in measurements of K x-ray emission inducted by electron bombardment [18] and in radioactive decay [19] are shown by triangles and circles, respectively. Theoretical $K\alpha$ hypersatellite shifts [17] are shown by the solid line.

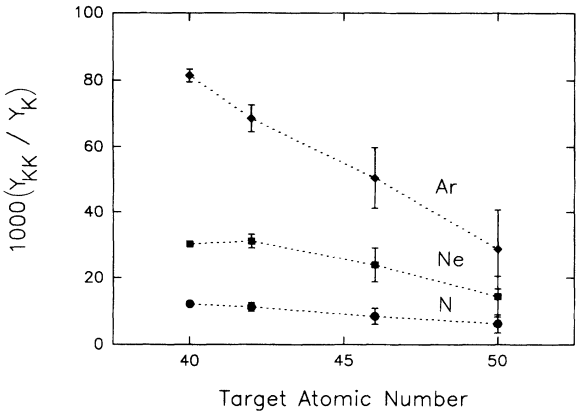

FIG. 11. Measured ratio of the $K\alpha$ hypersatellite yield to $K\alpha$ diagram plus satellite yield as a function of atomic number for Ar, Ne, and N projectiles.

than the equilibration thickness. The cross section obtained for Ge does indeed display the largest deviation in Fig. 8, thereby providing strong support for the above hypothesis.

Reliable energy analysis of the hypersatellite peaks was limited by the x-ray detector resolution to the four highest-Z targets investigated. The energy difference between the peak containing the $K\alpha$ diagram plus satellite lines and the peak containing the $K\alpha$ hypersatellite lines is shown for each of these four targets in Fig. 10. Under the assumptions that (a) the L-vacancy distribution is independent of the number of K vacancies and (b) the shift per L vacancy is approximately the same for $K\alpha$ x rays from the decay of single-K-vacancy states as from the decay of double-K-vacancy states, these energy differences may be compared with the hypersatellite shifts calculated by Chen, Crasemann, and Mark [17], which are shown by the solid line. The fact that the measured energy differences were independent of projectile Z supports the validity of the above assumptions. Hypersatellite shifts determined in measurements of K x-ray emission induced by electron bombardment [18] and by radioactive decay [19] also are shown in Fig. 10. Within experimental error, the present hypersatellite shifts, which are the only ones in this region of Z that have been measured for x-ray emission induced by heavy ion collisions, are in reasonably good agreement with the other experimental hypersatellite shifts and the theoretical predictions.

The ratios of the hypersatellite-to-satellite x-ray yields obtained for the Zr, Mo, Pd, and Sn targets using Ar, Ne, and N projectiles are shown in Fig. 11. The ratios for a particular target approximately increase quadratically with projectile Z. This behavior is consistent with a two-step mechanism for double-K-vacancy production, rather than a one-step (shake-off) mechanism, for which the yield ratios would be expected to increase linearly with Z_1.

VI. CONCLUSION

K-shell-ionization cross sections for 30-MeV/amu projectiles of H, N, Ne, and Ar incident on solid targets ranging from Al to Sn were determined from measured $K\alpha$ x-ray yields. Most of these collision systems lie outside the region of proven validity of the ECPSSR formulation, which, according to Basbas, Brandt, and Laubert [20], ranges from $Z_1/Z_2=0.03$ to 0.3 and $v_1/v_K=0.07$ to 2. Overall, the experimental cross sections displayed good agreement with the cross sections calculated using the ECPSSR theoretical formulation. The largest deviations between the experimental and calculated cross sections were of the order of 20% and occurred for Ar projectiles incident on Al and targets with Z_2 from 26 to 40. It was concluded that the latter deviations are probably attributable to the fact that over a significant fraction of the path length through the target, the Ar projectiles were not fully stripped of their electrons. This would cause the capture contribution to the total K-shell-ionization cross section to be smaller than predicted by the ECPSSR calculations.

ACKNOWLEDGMENTS

This work was supported by the Division of Chemical Sciences of the U.S. Department of Energy and the Robert A. Welch Foundation.

*On leave from the Department of Physics, Faculty of Science and Mathematics, University of Zagreb, Zagreb, Croatia.

†Present address: Institut Curie, 11 rue Pierre et Marie Curie, 75231 Paris CEDEX 05, France.

[1] G. Lapicki, J. Phys. Chem. Ref. **18**, 111 (1989).

[2] W. Brandt and G. Lapicki, Phys. Rev. A **23**, 1717 (1981).

[3] G. Lapicki and F. D. McDaniel, Phys. Rev. A **23**, 975 (1981).

[4] E. Liatard, J. F. Bruandet, F. Glasser, T. U. Chan, G. J. Costa, C. Gerardin, C. Heitz, M. Samri, and R. Selz, Z. Phys. D **2**, 223 (1986).

[5] M. P. Foratti and S. R. Piermattei, Nucl. Instrum. Methods **96**, 605 (1971).

[6] W. H. McMaster, N. K. Del Grande, I. H. Mallet, and J. H. Hubell, Lawrence Livermore Radiation Laboratory Report No. UCRL-50174, Sec. II, Rev. 1 (1969) (unpublished).

[7] C. M. Lederer and V. S. Shirley, *Table of Isotopes*, 7th ed. (Wiley-Interscience, New York, 1978).

[8] J. S. Hansen, J. C. McGeorge, D. Nix, W. D. Schmidt-Ott, I. Unus, and R. W. Fink, Nucl. Instrum. Methods **106**, 365 (1973).

[9] J. A. Bearden and A. F. Burr, Rev. Mod. Phys. **39**, 125 (1967).

[10] M. O. Krause, J. Phys. Chem. Ref. **8**, 307 (1979).

[11] R. Rice, G. Basbas, and F. D. McDaniel, At. Data Nucl. Data Tables **20**, 503 (1977).

[12] V. Horvat, R. L. Watson, G. Sampoll, T. Lotze, and B. Hill, Nucl. Instrum. Methods B **56/57**, 61 (1991).

[13] T. K. Li, R. L. Watson, and J. S. Hansen, Phys. Rev. A **8**, 1258 (1973).

[14] F. P. Larkins, J. Phys. B **4**, L29 (1971).
[15] F. Hubert, R. Bimbot, and H. Gauvin, At. Data Nucl. Data Tables **46**, 1 (1990).
[16] Y. Awaya, T. Kambara, Y. Kanai, A. Hitachi, T. Mizogawa, and K. Kuroki, Nucl. Instrum. Methods B **53**, 375 (1991).
[17] M. H. Chen, B. Crasemann, and H. Mark, Phys. Rev. A **25**, 391 (1982).
[18] S. I. Salem, Phys. Rev. A **21**, 858 (1980).
[19] G. Schupp and H. J. Nagy, Phys. Rev. C **29**, 1414 (1984) for $Z=37$; C. W. E. van Eijk, J. Wijnhorst, and M. A. Popelier, Phys. Rev. A **20**, 1749 (1979) for $Z=45$; V. Horvat and K. Ilakovac, *ibid.* **31**, 1543 (1985) for $Z=47$; C. W. E. van Eijk, J. Wijnhorst, and M. A. Popelier, *ibid.* **24**, 854 (1981) for $Z=49$; K. Ilakovac, M. Vesković V. Horvat, and S. Kaučić, *ibid.* **42**, 3984 (1990) for $Z=54$.
[20] G. Basbas, W. Brandt, and R. Laubert, Phys. Rev. A **17**, 1655 (1978).